5

Thermal Reduction of Graphene Oxide

Seung Hun Huh

Nanotechnology Convergence Lab,
Korea Institute of Ceramic Engineering and Technology (KICET),
South Korea

1. Introduction

In a two-dimensional carbon system for graphene (GP), three carbon electrons in four hybridized bonding electrons ($2s^12p_x^12p_y^12p_z^1$) form strong in-plane sp^2 bonds consisting of a honeycomb structure, and a fourth electron spreads out over the top or bottom of the layer as a π electron. The π electrons play an important role in the coupling interactions of multilayered GPs. A two-dimensionally spread C=C resonance structure and the hybridized electrons confined in GP are directly related to graphene's unique characteristics, such as its ballistic electron conduction, high thermal conduction, and high mechanical strength (Geim & Novoselov, 2007; Lee et al., 2008). These fundamental properties have been well studied using high-quality graphene produced by the "top-down" physical exfoliation (McAllister et al., 2007) and solvation-assisted exfoliation of graphite (Lotya et al., 2009) and GP thin films produced using chemical vapor deposition (Kim et al., 2009; Obraztsov, 2009).

Meanwhile, thermally reduced GP from graphene oxide (GO) (Gao et al., 2009; Jeong et al., 2009), produced from graphite using various chemical oxidation routes (Brodie, 1859; Hummers & Offerman, 1958; Hirata et al., 2004), has attracted considerable attention as a potential material for use in various industrial applications such as photovoltaic cells, capacitors, sensors, and transparent electrodes (Geim & Novoselov, 2007; Stoller et al., 2008; Wang et al., 2008; Liu et al., 2009). This is because of not only its potential in significantly lowering the cost of mass-produced graphene but also the simple, nonchemical, thermal conversion of GO powder or film to GP powder or film, respectively (Titelman et al., 2005; (a) Jeong et al., 2009; (b)). However, the thermal reduction of GO is a very complex phenomenon because of the thermal-energy-induced multistep removal processes of intercalated H_2O molecules and oxide groups of –COOH (carboxyl group), –OH (hydroxyl group), and >O (epoxy group). It should be noted that in chemical reduction, individual GO sheets in the solution phase are chemically reduced by the strong chemical base (Titelman et al., 2005; Ju et al., 2010). Therefore, the thermal reduction of GO and resultant GP needs to be studied in great detail.

In this research, X-ray diffraction (XRD) was used to probe the temperature-dependent evolution of the interlayer distance (d_{002}) of GO/GP films and powders within temperature ranges of room temperature (RT) to 1000°C and RT to 2000°C, respectively. XRD results show a detailed thermal reduction of GO with the removal of intercalated H_2O molecules and oxide groups, defect formation, lattice contraction and exfoliation mechanisms of the GO/GP sheets, the folding and unfolding of the GO/GP layers, and a bottom-up layer stacking toward bulk graphite.

2. Experimental

Graphene oxide was prepared using a modified Hummers' method (Hirata et al., 2004). First, 5 g of natural graphite (99.995%, Alfa), 3.75 g of $NaNO_3$ (99%, Aldrich), and 310.5 g of H_2SO_4 (96%) were mixed in a 10-L pyrex reactor with a water cooling system; this mixture was then stirred for 30 min. Next, 22.5 g of $KMnO_4$ (99%, Aldrich) was carefully added to this mixture for 1 h. The resultant mixture was stirred for 5 days at room temperature, after which 5 L of a H_2SO_4 aqueous solution (5%) was slowly added over a 1 h period. After stirring for 2 h, 150 g of H_2O_2 (30%, Aldrich) was added to the mixture. Upon centrifugation, the GO slurry at the bottom was washed with a 3%-H_2SO_4/0.5%-H_2O_2 solution and then rewashed with deionized water (Ju et al., 2010).

The final GO was obtained as a slurry or colloidal solution, which was then spin-coated on a flat Pt XRD holder and dried at RT. The GO thickness was approximately 300 to 500 nm. The GO film mounted on the Pt XRD holder was measured in situ in a vacuum (~10^{-3} torr, obtained with a rotary pump) at RT to 1000°C using a high-temperature XRD instrument (RIGAKU, D/MAX-2500, λ = 1.54056 Å (Cu K_α)). The heating rate was 5 °C/min.

To obtain the GO powder, the GO slurry was dried in a vacuum oven at 60°C for 24 h. Dried GO powder (the brown color in Fig. 1b) mounted on a crucible was introduced into a quartz furnace and thermally treated at RT to 2000°C for 1 h under a flow of laminar N_2 gas (99.999%). The heating rate and N_2 flow rate were 5 °C/min and 50 ml/min, respectively. GO and GP were further characterized using a field-emission scanning electron microscope (FE-SEM: JEOL, JSM 6700F), FE-transmission electron microscope (FE-TEM, JEOL, JEM-2000EX (200 keV)), Fourier transform infrared spectroscope (FT-IR; Jasco 4100), and a Cs-corrected FE-TEM (JEOL/CEOS) was used for measuring the in-plane carbon lattices. The obtained products are denoted as $GP_{temperature}$, e.g., GP_{200} or GP_{1000}. The interlayer distances (d_{002}) are denoted as $d_{temperature}$, e.g., d_{RT} or d_{2000}.

3. Results and discussion

3.1 XRD theory and concept of interlayer distances of graphene and graphene oxide

The principle of XRD for materials is based on Bragg's law (Cullity, 1978), and it is expressed by

$$n\lambda = 2d_{(hkl)}\sin\theta \qquad (1)$$

where λ is the wavelength of the X-ray, θ is the scattering angle, n is an integer representing the order of the diffraction peak, d is the interplane distance of the lattices, and (hkl) are Miller indices. If (002) planes of graphite or multi-layered graphene are given as in Fig. 1a, the interlayer distance is denoted as d_{002}. The incoming X-rays are specularly scattered from each GP plane. Since the angle θ between the GP plane and the X-ray beam results in a path-length difference that is an integer multiple *n* of the X-ray wavelength λ, X-rays scattered from adjacent individual GP planes will combine constructively. Therefore, the XRD peak of the (002) facet of GP gives rise to a critical d_{002} value as well as the information required for the lattice size and quality. The GP thickness can be estimated using Sherrer's equation (Cullity, 1978), which is expressed by

$$D_{002} = K\lambda / B\cos\theta \qquad (2)$$

where D_{002} is the thickness of crystallite (here, GP thickness), K is a constant dependent on the crystallite shape (0.89), λ is the X-ray wavelength, B is the full width at half maximum (FWHM), and θ is the scattering angle. From Sherrer's equation, the number of GP layers (N_{GP}) can be obtained using the following equation (Ju et al., 2010):
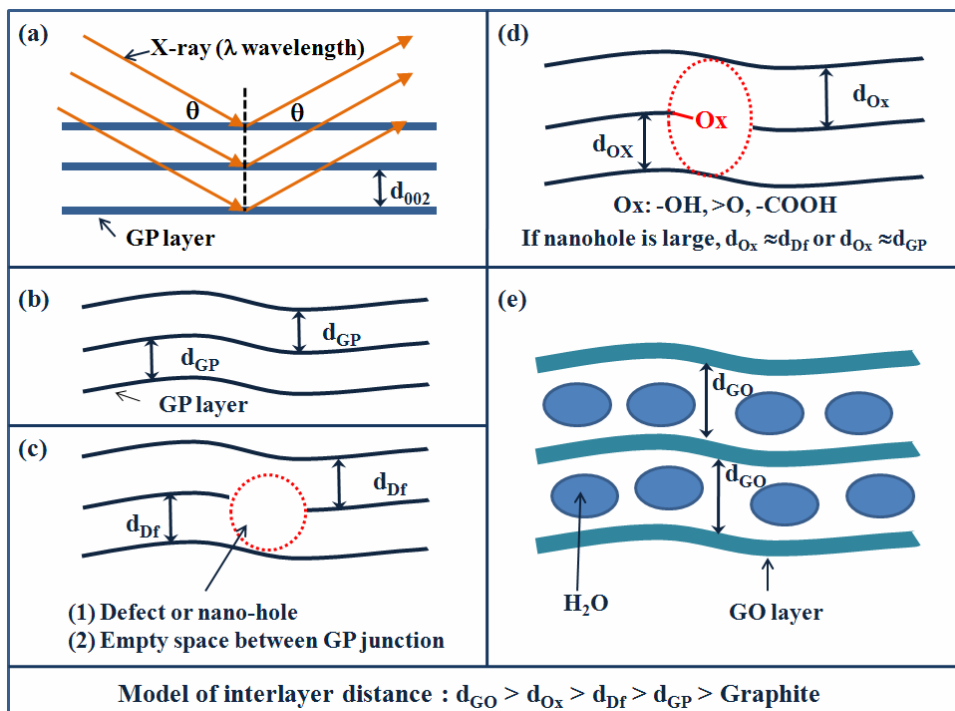
$$N_{GP} = D_{002} / d_{002} \tag{3}$$

Fig. 1. Bragg's law for GP or graphite (002) planes (a), and models for d_{002} of GO (e) and thermally reduced GP (b-d). In this model, the order of interlayer distance becomes graphite < d_{GP} < d_{Df} < d_{Ox} < d_{GO}.

To understand the XRD pattern formed during the GO reduction as well as the resultant GP, a simple, intuitive concept for various types of interlayer distances of graphene and graphene oxide is considered, as shown in Figs. 1b through 1e. Because GP layers have intrinsic nanocurvature distortions (Fig. 1b) (Fujimoto, 2003; Li et al., 2007) existing in a two-dimensional single crystalline structure (McAllister et al., 2007; Gosselin et al., 2009), the interlayer distance of GP (d_{GP}) is slightly larger than that of bulk graphite. The reported d_{GP} and graphite are ~3.4 (Stankovich et al., 2007) and 3.348–3.360 Å (Li et al., 2007), respectively. Because GO has many defects or nanoholes, it is reasonable that thermally reduced graphene would also have many defects and nanoholes (d_{Df}) (Fig. 1c). Therefore, GO and GP can have oxide groups of C–Ox with an sp³ bond in their defects and nanoholes (d_{Ox}) (Fig. 1d). Graphene oxide has the largest interlayer distance (d_{GO}) because of its intercalated H_2O molecules and various oxide groups (Fig. 1e). The d_{GO} value is in the range

of ~5 to 9 Å, depending on the number of intercalated water molecules. It is rational to assume that the interlayer distance order is $d_{GO} > d_{Ox} > d_{Df} > d_{GP} >$ graphite. If defects in the layer are sufficiently large, oxide groups and H_2O molecules can be considered to exist in the empty space; thus, the order is $d_{Ox} \approx d_{Df}$ or $d_{Ox} \approx d_{GP}$. On the basis of a model with various interlayers, we expect that graphene oxide has an intermediate structure with d_{Ox} and d_{Df} during thermal reduction, and through bottom-up layer stacking, the resultant graphene evolves toward graphite as crystal growth with the removal of d_{Ox} and d_{Df}.

3.2 Images of GO/GP film and GO/GP powder

Figure 2a shows a digital image of GO slurry. Figure 2b shows an FE-SEM image of a GO film with a thickness of ~300 to 500 nm, and demonstrating a soft carpet-like morphology (c). An FE-TEM image of a GO film coated on a Cu TEM grid (Fig. 2d) shows a layered AB-stacked structure. However, GP films obtained after thermal annealing at 1000°C have surface microcracks and a shrunken thickness, as shown in Figs. 2e and 2f, respectively. Figure 2g shows a digital image of dried GO powder. After undergoing thermal reduction at 1000°C, the brown-tinted GO lumps turn into fine black GP powder (Fig. 1h).
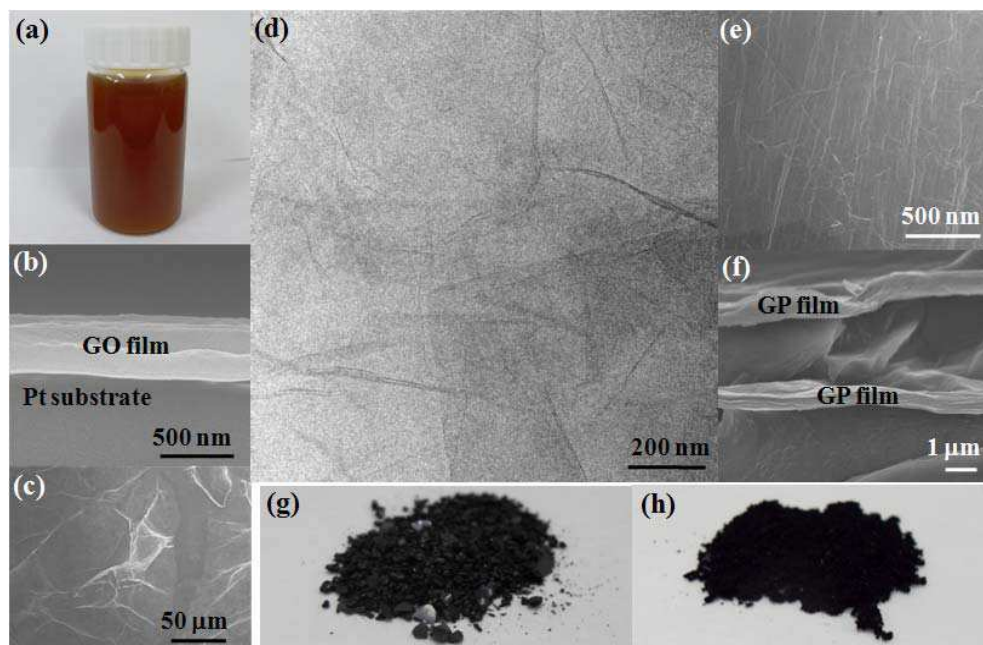

Fig. 2. A digital image of GO slurry (a), dried GO powder (g), and thermally reduced GP powder (h). FE-SEM images of GO films (b, c), thermally reduced GP films (e, f), and FE-TEM image of GO film (d).

3.3 Temperature-dependent XRD patterns of GO and GP films

All temperature-dependent XRD patterns of GO/GP films measured within the range of RT to 1000°C are completely plotted in Fig. 3. At increasing temperatures, the (002) peak of a GO film (left side) moves continuously toward the right with a variance of intensity and FWHM.
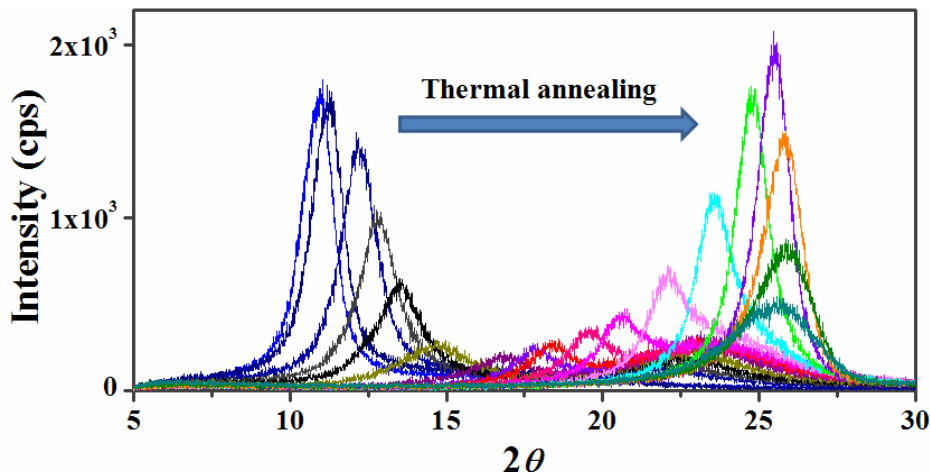
Fig. 3. Total plot for measured in situ XRD patterns of GO/GP films obtained at RT to 1000°C.

The individually-represented XRD spectrum shows important information regarding the detailed temperature-dependent evolution of (002) peaks, as shown in Fig. 4. A GO film with an AB stacked structure (Li et al., 2007; (b) Jeong et al., 2008) shows a typical XRD pattern with a strong and sharp (002) peak at 2θ = ~11° (Fig. 4a). The GO (002) peak gradually shifts to the right with an increase in temperature and yields three types of (002) peak series. The first peak series (Peak I) is the main change during the thermal reduction of graphene oxide and shows a gradual shift to the right. The d_{GO} and d_{1000} values for Peak I are 8.071 (Fig. 4a) and 3.453 Å (Fig. 4t), respectively. In the second peak series (Peak II), a peak at 2θ = ~24° emerges at 140°C (Fig. 4d), with a slight shift to the right within the temperature range of 140–600°C. Importantly, all Peak II values have a larger FWHM than those of Peak I. The d_{140} and d_{500} values for Peak II are 4.034 (Fig. 4d) and 3.602 Å (Fig. 4n), respectively. Significantly, Peak II is combined to Peak I at 600°C (Fig. 4o). The combined peak of GP_{600} is very sharp, and d_{600} is 3.593 Å. The combined GP_{600} is gradually moved to the right with an increase in temperature, along with a broadening FWHM. However, peaks above 700°C show a long-tailed structure because of small portions of peaks at 2θ = ~23–24°, which is denoted as a third peak series (Peak III). The centers of Peak III are changed slightly, and their d_{002} values are far from graphite d_{002}. From these results and from the fact that the intensities of all Peak III values are much lower (less than 100 cps) than those of Peak I and Peak II, it is assumed that Peak III is amorphous-like carbon comprising many defects, folding structures, impurities, and sp^1, sp^2, and sp^3 hybridization structures. It should be noted that GP_{1000} measured in situ at 1000°C (Fig. 4s) shows a very broad and left-shifting structure compared to GP_{800} because of typical Debye-Waller effects induced by atomic thermal vibration; thus, after the cooling of GP_{1000}, GP_{RT} is obtained after an XRD measurement at RT (Fig. 4t). The d_{002} and FWHM values, as well as induced errors, are summarized for both Peaks I and II in Appendix 1.

Figures 5a and 5b show a plot of the d_{002} and FWHM values for both Peak I (solid blue circles) and Peak II (hollow red circles), respectively, on the basis of the fitting (Lorentzian function) XRD patterns shown in Fig. 4. The plots show four temperature-dependent

tendencies: (1) RT–130°C, (2) 140–180°C, (3) 180–600°C, and (4) 600–1000°C. Within the RT–130°C zone, only Peak I appears. The mild reduction of d_{002} values and unchanging FWHM (or a very slight increase) are attributed to a mild vaporization of intercalated H_2O molecules. Within the 140–180°C zone, both Peaks I and II appear. For Peak I, the d_{002} values are largely reduced, and the FWHM values are maximally broadened. This is because of a drastic vaporization of intercalated H_2O molecules ((a) Jeong et al., 2009; (b)). In this process, the sizes of the GO crystals estimated using Sherrer's equation are reduced as the crystals are exfoliated during a drastic escaping of H_2O gases from stable GO-layered lattices, resulting in Peak II with very broad FWHM. For Peak II, the d_{002} and FWHM tendencies are similar to those of Peak I. Thus, partial H_2O molecules exist in the exfoliated GO and are then vaporized in a temperature range of 140–~180°C. Within the 180–600°C zone, the d_{002} and FWHM values are continuously reduced for both Peak I and Peak II. This is due to the removal of the main oxide groups of COOH. However, above 600°C, although the d_{002} values are continuously contracting and approaching graphite d_{002}, the FWHM values are gradually broadening. This is a very complex phenomenon related to lattice relaxation and disordering, which is detailed in section 3-5.
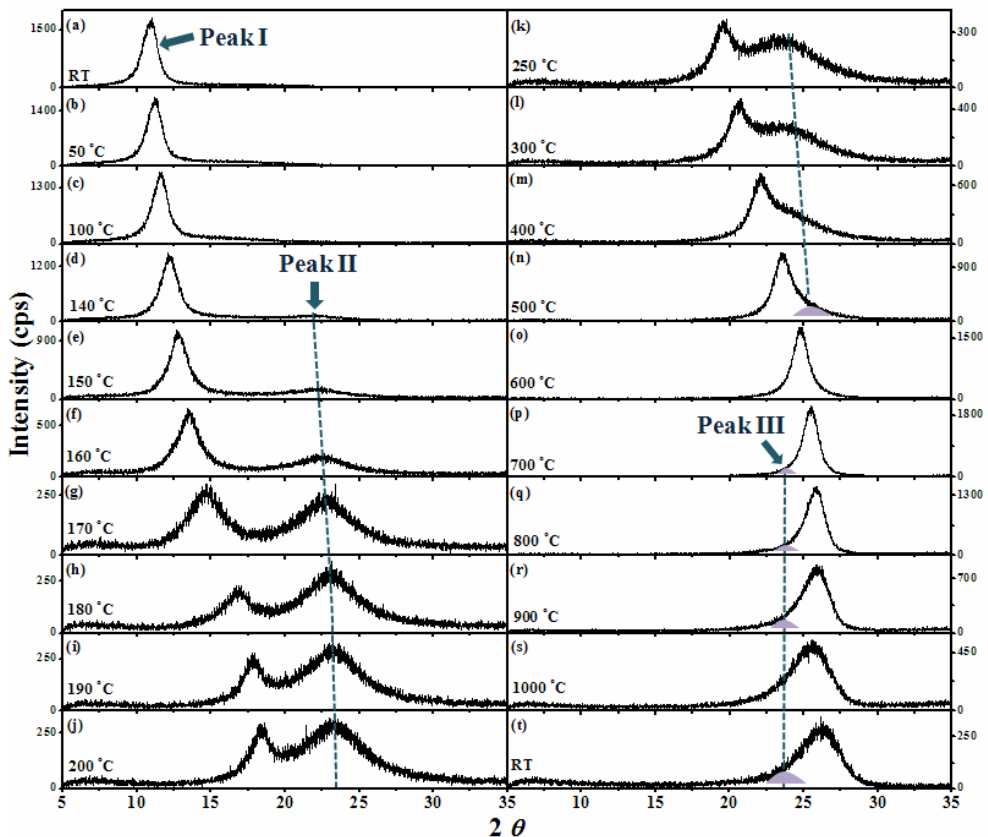

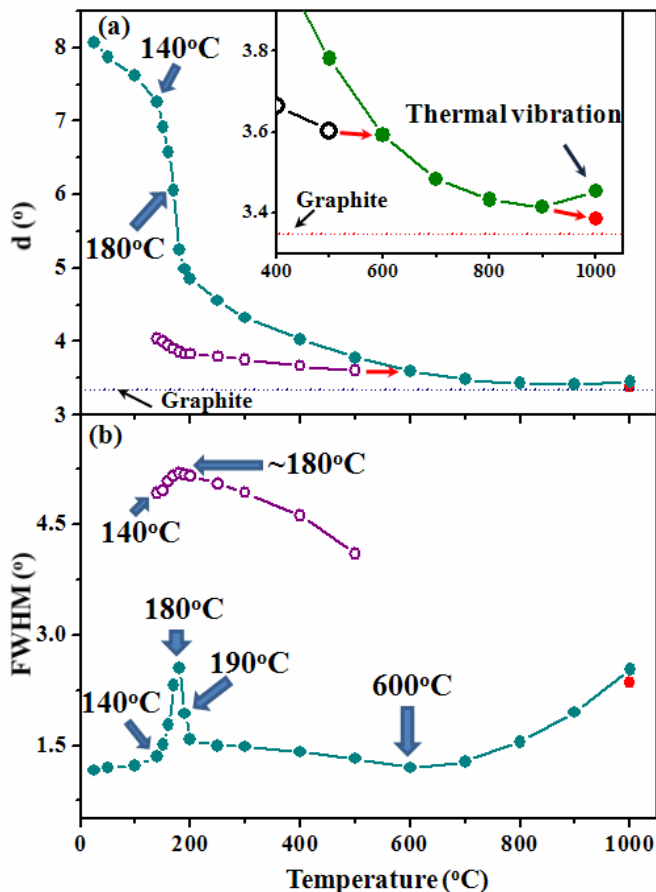Fig. 4. Individual XRD plot for Fig. 3.

Fig. 5. FWHM (a) and d_{002} (b) plots for XRD patterns of Fig. 4. The inset shows a magnified image of (a).

3.4 Temperature-dependent XRD patterns of GO and GP powders

The XRD patterns of GO/ GP powders (Fig. 6) appear to be totally different from those of GO/GP films with a range of RT–1000°C because there is only one peak type with a broad FWHM. However, the peaks are very similar to Peak II of GO/GP films, as shown in the d_{002} and FWHM plots of Fig. 7. As a result, GP_{200} and GP_{400} have a fully exfoliated structure, such as that in Peak I. Full exfoliation of GO powder at a relatively low temperature of 200°C depends on the GO drying process. To obtain a GO powder, a GO slurry is extensively dried above 60°C in vacuum. The d_{002} value (7.131 Å) of the obtained GO powder is smaller than d_{100} (7.611 Å) and is similar to d_{140} (7.259 Å) of a GO film (note that Peak II emerges at 140°C in a GO film).

Therefore, extensively dried GO powder can be fully exfoliated when a large number of intercalated H_2O molecules escape at 200°C. Importantly, along with similar tendencies compared to a GP film, the temperature-dependent XRD patterns of thermally reduced GPs
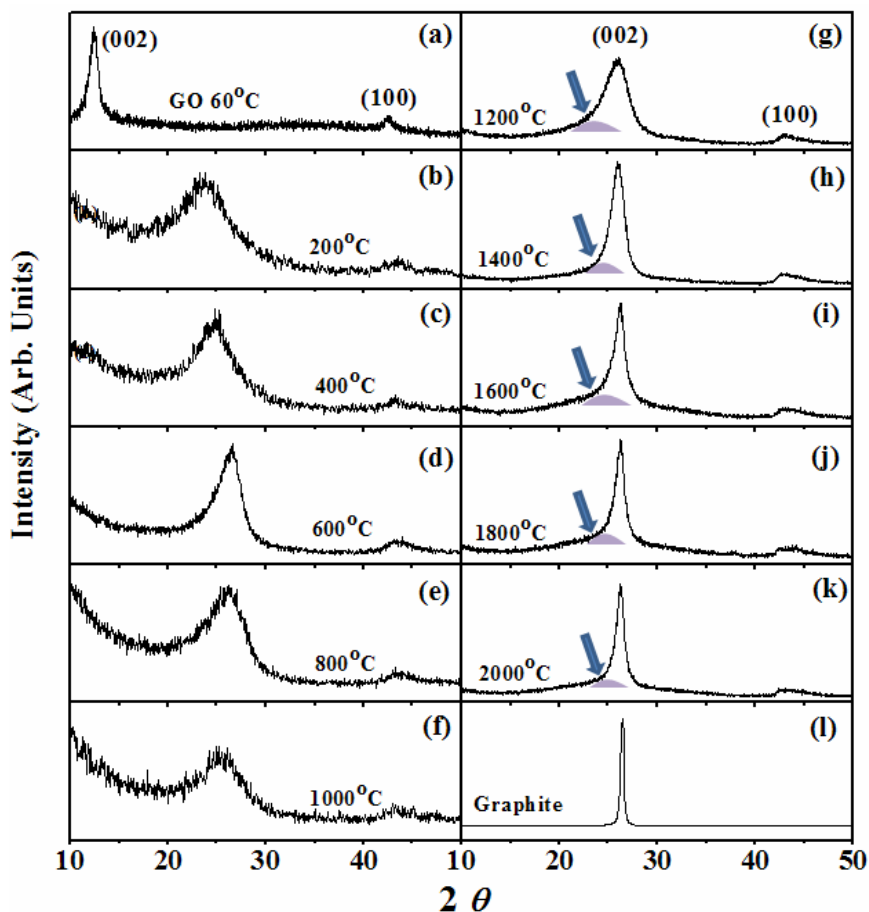
Fig. 6. XRD patterns of GO/GP powders obtained after thermal annealing at RT to 2000°C.

from RT to 1000°C have two different zones with their boundary appearing at 600°C in FWHM and d_{002} (Figs. 7a and 7b and Figs. 7c and 7d). FWHM sharpens as $GP_{200} \rightarrow GP_{400} \rightarrow GP_{600}$ and then broadens as $GP_{600} \rightarrow GP_{800} \rightarrow GP_{1000}$, shrinking as $GP_{200} \rightarrow GP_{400} \rightarrow GP_{600}$ and growing as $GP_{600} \rightarrow GP_{800} \rightarrow GP_{1000}$. Above 1000°C, the quality of thermally reduced GP powder increases because of the decreasing FWHM and d_{002} approaching bulk graphite. Furthermore, peaks above 1200°C show a long-tailed structure because of small portions of peaks at $2\theta = \sim23$–$26°$, which is considered to be a similar structure as Peak III in GP films. The measured d_{002} and FWHM values, along with induced errors, are summarized in Appendix 1.

3.5 FT-IR, Raman, and FE-TEM results for GO and GP powder

From the FT-IR spectra of GO and GP powder (Fig. 8), typical peaks of intercalated free H_2O molecules are seen at ~3250 cm^{-1}, and those of bound H_2O molecules are observed at ~1612 cm^{-1} and ~1383 cm^{-1}; peaks corresponding to COOH, OH, and epoxide groups and in-plane
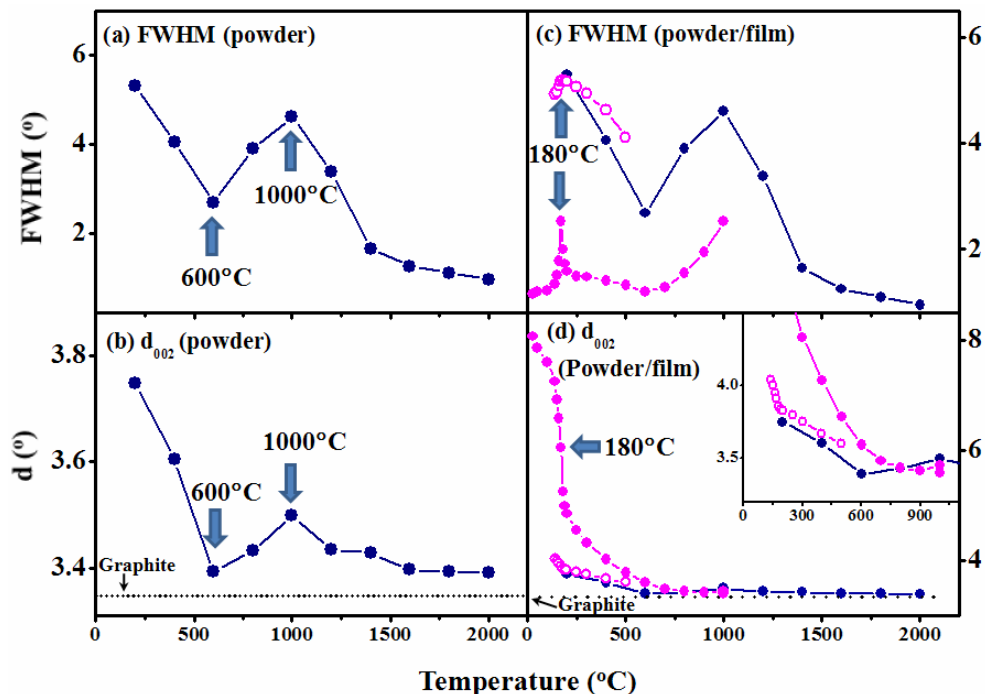
Fig. 7. FWHM (a) and d_{002} (b) plots, and FWHM (c) and d_{002} (d) co-plots for GO/GP films and powders. The inset shows a magnified image of (d).

C=C bonds are also observed at ~1730, ~1200, ~1040, and ~1510 cm^{-1}, respectively. FT-IR spectra indicate five types of GO and GP thermochemical reactions: (i) vaporization of intercalated water molecules at RT to 200°C, (ii) removal of most carboxyl groups (–COOH) at ~200–600°C, (iii) removal of residual carboxyl and partial hydroxyl groups (C–OH and O–H) at ~800°C, (iv) near removal of residual hydroxyl groups and partial removal of the epoxide group (>O) at ~1000°C, and (5) the removal (cracking) of aromatic C=C bonds at 1000°C.

Meanwhile, the Raman spectra (Fig. 9) show three different regimes of the D/G ratio (disorder/order carbon), with their boundaries between 800 and 1000°C (Fig. 10). This ratio remains at RT to 800°C and then drastically increases as $GO/GP_{200-800}$ (~1.5) → GP_{1000} (~2.1), which implies that the disordering portion of the two-dimensional carbon backbone is increased in this temperature range. The XRD patterns and Raman spectra taken together indicate that a change from $GP_{200-600}$ to GP_{800} with a decrease in d_{002} and an increase in FWHM is not related to the number of defects, whereas a change from GP_{800} to GP_{1000} with an increase in d_{002} and an increase in FWHM is largely affected by an increase in the number of disordered carbons.

Although GP_{600} has a partial carboxyl group and numerous hydroxyl and epoxide groups, as shown in the FT-IR spectra, it has high-quality crystallinity with d_{600} = 3.392 Å, which is closest to a typical GP (d_{002} = 3.4 Å). This means that most of the residual oxide groups exist on the edge or interlayer empty space of GP_{600}; therefore, the oxide groups are not largely
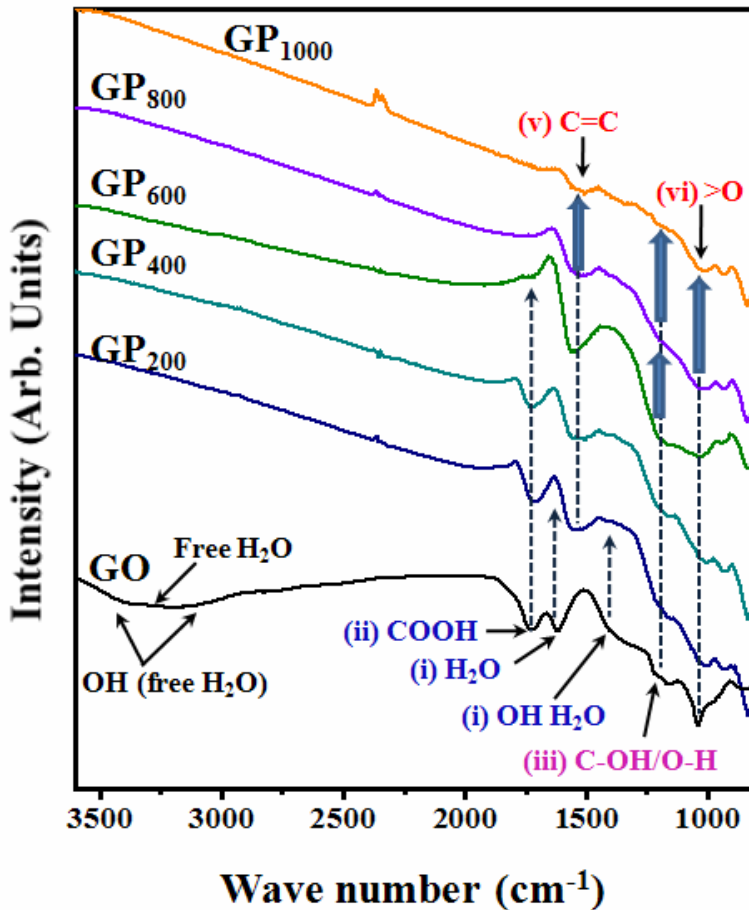
Fig. 8. FT-IR spectra for GO, GP_{200}, GP_{400}, GP_{600}, GP_{800}, and GP_{1000} samples.

affected by the layered stacking structure. GP_{800} has poorer crystallinity than GP_{600} (see the d_{002} and FWHM values). However, Raman data shows that both GP_{600} and GP_{800} have a similar D/G ratio as well as a similar Raman pattern. The combined XRD and Raman data in the range of 600–800°C are very abstruse. To solve this problem, two combination effects are supposed: a lattice relaxation mechanism and the detachment of disordered carbon. At 600–800°C, residual carboxyl groups and a partial hydroxyl group are detached.

Although the carboxyl groups do not require an additional carbon source to decompose into CO_2, the hydroxyl groups need a carbon source to yield CO gas (Figueiredo et al., 1999). If the carbon in CO gas comes from an ordered aromatic C=C structure, the D/G ratio will increase. If the carbon in CO gas comes from a disordered C–C structure, the D/G ratio will be unchanged. Many disordered carbons already exist in GO and $GP_{200–600}$ as shown in the Raman spectra (D/G = ~1.5). Therefore, the probable explanation for the unchanging Raman spectra of GP_{600} and GP_{800} is that the carbon in CO gas is produced from disordered carbon located at the edges and boundaries of nanoholes and empty spaces. The reason for
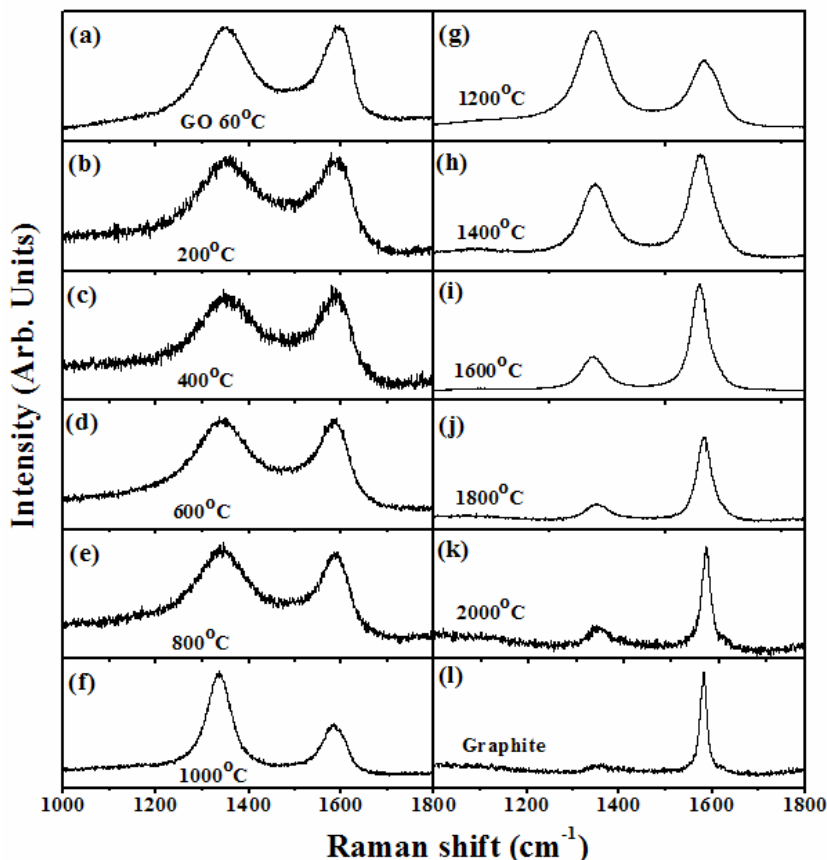
Fig. 9. Corresponding Raman spectra samples for XRD patterns of Fig. 6.

degradation of crystalline quality as $GP_{600} \rightarrow GP_{800}$ is explained by the lattice relaxation mechanism of GP_{600}; CO_2 and CO gases produced from the removal of residual carboxyl and partial hydroxyl groups, respectively, have high vibration and kinetic energy and pass through stable layers of GP_{600}. However, GP_{800} is considered to be a relatively good GP species because it has the smallest amount of oxide under an unchanging number of defects. As shown in a representative image of a Cs-corrected FE-TEM, a six-layered structure is observed at the edge of GP_{800} (Fig. 11a), and in-plane ordered lattice structures in the flat zone between the microfolding areas are also observed (Fig. 11b).

GP_{1000} has the largest amount of disordered carbon as shown in the Raman spectra. This is explained by the cracking of two bonds of >O, which causes the simultaneous destruction of adjacent C=C aromaticity, as shown in the FT-IR spectrum. Furthermore, broad D and G Raman peaks sharpen above 1000°C because of the thermal annealing effect. Between 1000 and 2000°C, the D/G ratio is continuously decreased, and it then approaches raw graphite material, which is in accord with XRD data on the basis of the fact that the crystalline quality increases and the crystal growth of GP layers is very effective owing to the thermal annealing effect, implying an accompaniment with the removal of d_{Ox} and D_{Df} (Fig. 1).
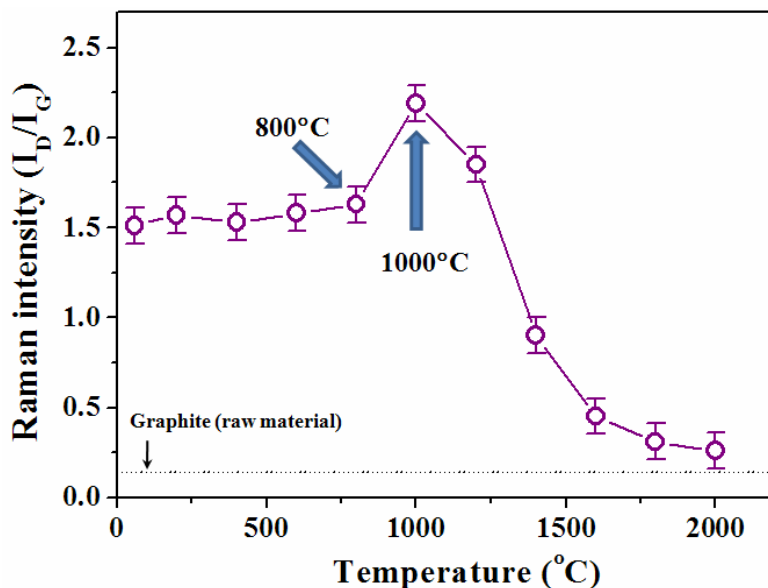
Fig. 10. Plot of Raman intensity ratio, I_D/I_G, of Fig. 9.

Based on equation 3, if the defects are offset for $GP_{200-800,1400-2000}$, the numbers of layers of GP_{200}, GP_{400}, GP_{600}, GP_{800}, GP_{1400}, GP_{1600}, GP_{1800}, and GP_{2000} are estimated to be 4.1, 5.5, 8.3, 6.1, 9.3, 12.3, 14.0, and 16.3, respectively. In this estimation, GP_{1000} and GP_{1200} are exceptions because of the existence of disordered carbon in an amount larger than the base GO powder. Further, we supposed that residual oxide groups do not exist in a well-developed interlayer space, but rather at the edges or nanoholes. This supposition is reasonable given that the maximum gap of 0.3 Å between $d_{200-800,1400-2000}$ = 3.390–3.747, and $d_{graphite}$ = 3.348 Å is too small to contain the ~1.25-Å minimum epoxy group (Giordano et al., 1988; Mkhoyan et al., 2009) or the ~2.75-Å of H_2O molecules (Graziano, 1998). However, various interlayer distances are explained by the contribution of d_{Df} and d_{Ox}, as shown in Fig. 1. Furthermore, because the estimated number of layers in $GP_{1400-2000}$ is very large, they are considered to have intermediate properties between typical graphene (less than 10 layers) and graphite.

3.6 Folding and unfolding processes of GO and GP powders

It is noteworthy that from the FE-SEM (left) and FE-TEM images (right) (Fig. 12), we observed both folding and unfolding graphene: (1) $GP_{200-600}$ with severely wrinkled or folded structures in both macroscopic and microscopic views (Figs. 12a–12c) and (2) GP_{800} with slightly unfolded structures (Fig. 12d) and GP_{1000} with a considerably unfolded and flat structure except for microwrinkling (Fig. 12e).

$GP_{200-600}$ have crater-like macropores surrounding the thick folded sheets owing to the vaporization of intercalated H_2O molecules, as shown in Figs. 12a–12c. It is possible that during the drastic exfoliation of AB-stacked GO, individually exfoliated GO sheets are unstable owing to a large number of defects (D/G = ~1.5), surface/edge dangling bonds, high surface-to-volume ratio, and thermodynamic instability as intrinsic properties of two-dimensional crystal; subsequently, for better stability, they tend to be coupled with each
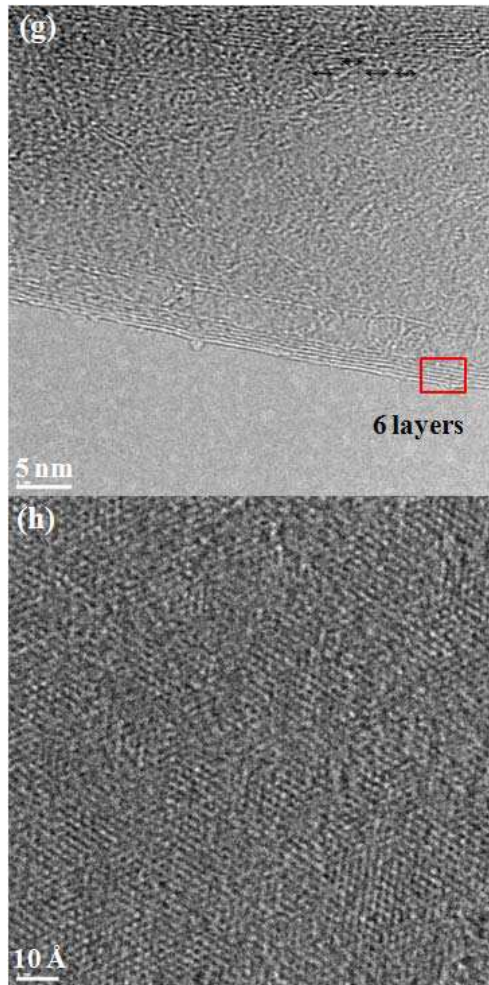
Fig. 11. Cs-corrected, high-resolution FE-TEM images for thermally reduced GP$_{800}$ powder: six-layered structures located at the edge (a) and in-plane ordered carbon structure (b).

other through a van der Waals interaction. In this layer-coupling process, interlayer partial chemical or hydrogen bonds may be formed because of a large number of defects, dangling bonds, and O/H atoms, which are the driving force behind microscopic and macroscopic folding (Figs. 12a–12c). It should be noted that microscopic folding is an intrinsic characteristic of GP layer produced via chemical reduction and top-down physical exfoliation. Severely macrofolded GP$_{200-600}$ with porous structures are partially unfolded during the formation of GP$_{800}$ (Fig. 12d) and largely unfolded at 1000°C. The unfolding process of GP$_{1000}$ may be attributed to the coincident detachment of interlayer chemical and hydrogen bonds owing to both the effects of thermal annealing and the removal of C/O species. A schematic of the folding and unfolding processes during the thermal reduction of GO is summarized in Fig. 13.
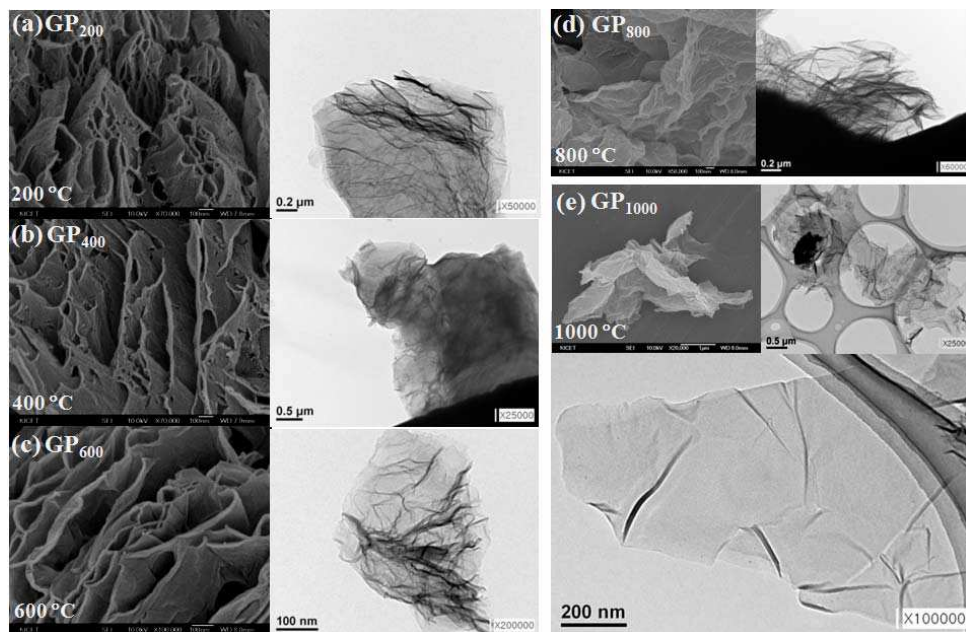
Fig. 12. FE-SEM (left) and FE-TEM images (right) for GP_{200} (a), GP_{400} (b), GP_{600} (c), GP_{800} (d), and GP_{1000} (e).
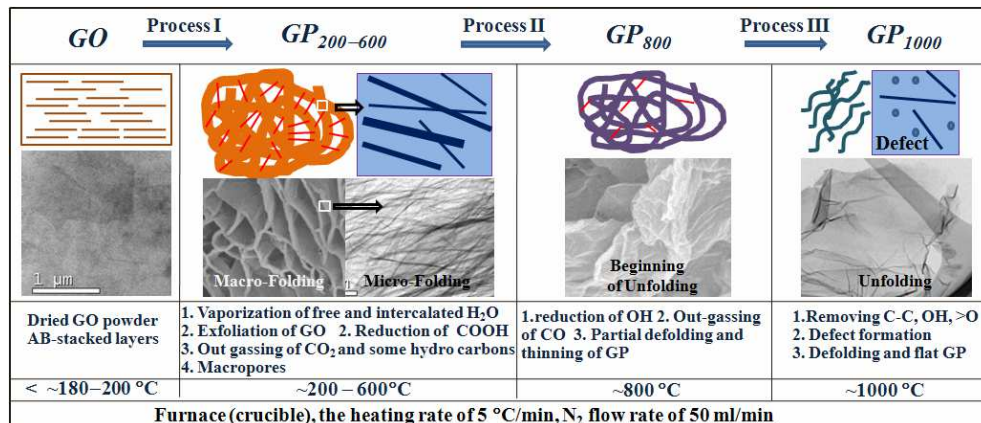
Fig. 13. Schematic diagram of folding and unfolding processes of $GP_{200-600}$, GP_{800}, and GP_{1000}.

3.7 Proposed model for thermal reduction of GO film and powder

From the XRD, FT-IR, Raman, FE-SEM, and FE-TEM results for GO/GP films and powders, a thermal reduction process for GO using five critical temperatures of 140, 180, 600, 800, and 1000°C is proposed, as shown in the schematic diagram of Fig. 14. In this model, the d_{002} value of large-sized GO crystal is gradually contracted within the range of RT–130°C during mild vaporization of intercalated H_2O molecules (S_1 state). However, the d_{002} value is

greatly reduced within 140–180°C owing to a drastic vaporization of intercalated water molecules (S_2), along with a partial exfoliation of GO sheets (S_7). The GO (S_2) and exfoliated GO (S_7) gradually reduce their lattices in the range 180–600°C because of the removal of the main carboxyl groups (S_3). Within 600–800°C, a partial lattice relaxation with a broadening FWHM occurs owing to out-gassing formed from residual carboxyl and partial hydroxyl groups ($S4$). Within 800–1000°C, a large number of defects are produced during the removal of the epoxide group, along with in-plane C=C cracking ($S5$). Within 1000–2000°C, bottom-up layer stacking as crystal growth occurs with a decreasing number of defects ($S6$). However, the thermal reduction processes for the GO films and powders always yield small amounts of amorphous-like structures around 2θ = ~23–25° within 140–2000°C, which is explained by the complex folding structures, defects, impurities, and sp^1, sp^2, and sp^3 hybridization. Furthermore, folding and unfolding processes occur between $GP_{200-600}$ and $GP_{800-1000}$ depending on the presence of interlayer partial chemical and hydrogen bonds.
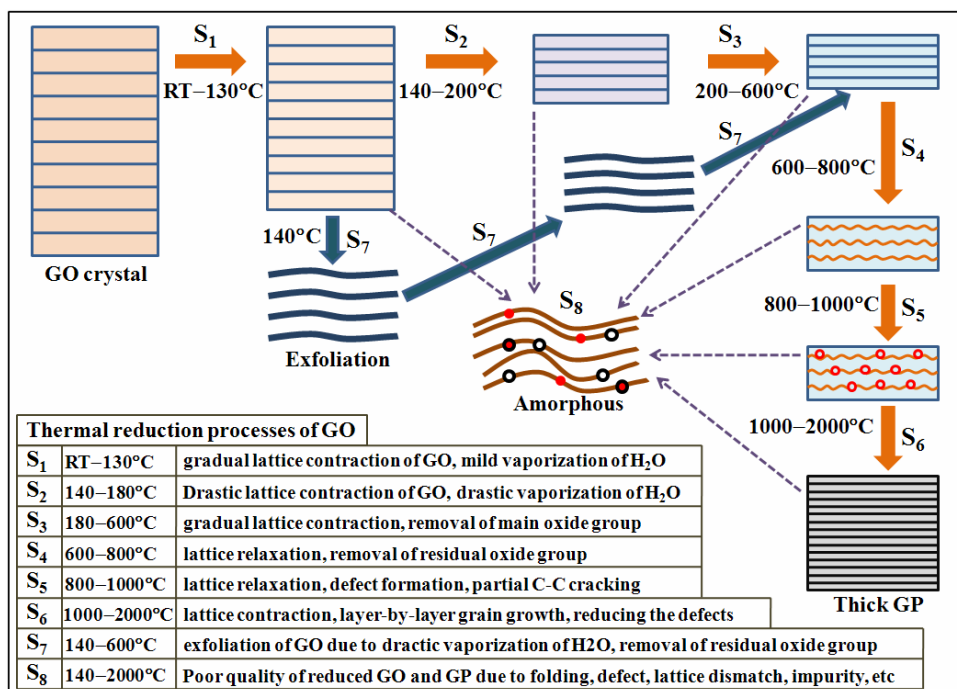

Fig. 14. Schematic diagram of thermal reduction process of GO in the range of RT to 2000°C.

3.8 Application of partially reduced GO film for dye-sensitized solar cell

Graphene oxide cannot be used as a catalytic film in a dye-sensitized solar cell (DSSC), because it is hydrophilic and water-soluble. A pure hydrophobic GP film is also not a good candidate for a catalytic film in a DSSC, because it is easily destroyed during the forced electric-field-induced penetration of iodide (I) ions. However, partially reduced GO shows a relatively good catalytic property. Figure 15a shows an XRD pattern for a partially reduced GO film with a partially reduced GP structure, which is produced by careful heating on a hot plate at ~250–300°C for a short duration of around 2 min in air. The partially reduced

GO film has an intermediate contact angle of $\alpha = 59°$ (water droplet film) (Fig. 15b) between GO of $\alpha = 7°$ (Fig. 15c) and GP_{600} of $\alpha = 85°$ (Fig. 15d). Although this film maintains the hydrophilic property caused by a partial GO structure, it is water-insoluble owing to sections of reduced GP. We obtained a solar power conversion efficiency (η) of more than 2%. Although η is relatively lower than that of a DSSC with a platinum catalytic thin film (6.0%) under the conditions of this experiment, it is higher than that of a DSSC without a catalysis (0.74%) and those of other reported types of DSSC (0.84%) (Liu et al., 2009) and organic solar cell (1.1%) with conductive graphene electrode (Wang et al., 2008). The catalytic effect is explained by the effect of the ion channel through the sections of hydrophilic GO. This result implies that as an alternative to an expensive Pt catalyst, partially reduced GOs have the potential for use in a DSSC as a cheap catalytic thin film.
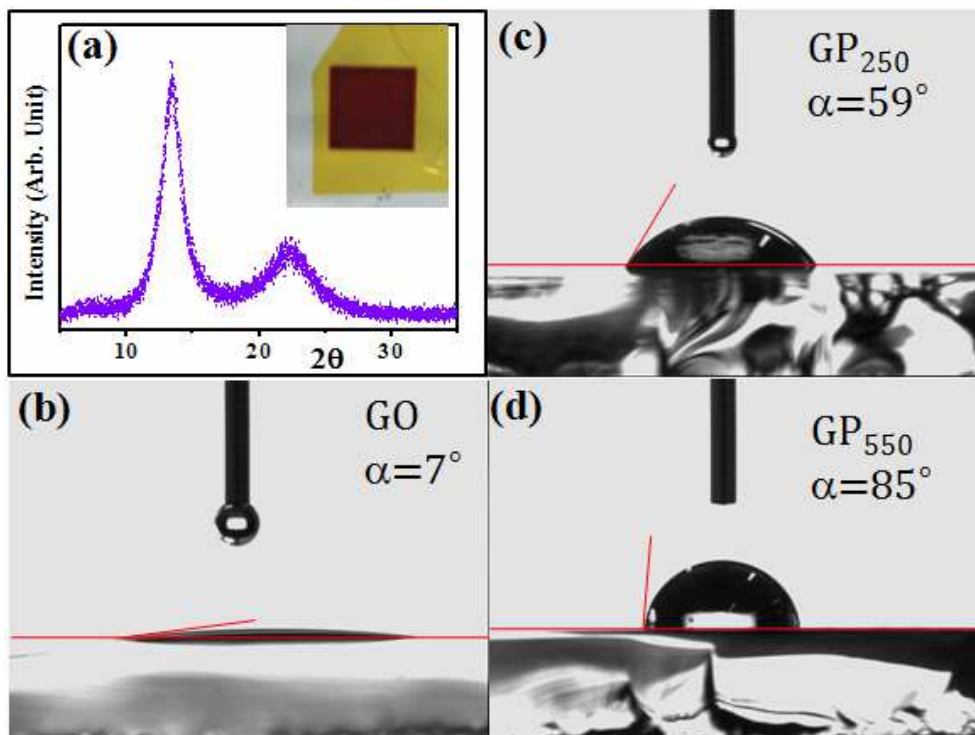

Fig. 15. XRD pattern of partially reduced GO film (a) used as a catalytic film of a DSSC (inset). Digital images of contact angles between water droplets and GO film (b), partially reduced GO (c), and GP (d).

4. Conclusion

Using XRD, Raman, FT-IR, FE-SEM, and FE-TEM results, a thermal reduction process of graphene oxide within a temperature range of RT to 2000°C was investigated in detail. The thermal reduction process has six important temperature zones, RT–130°C, 140–180°C, 180–600°C, 600–800°C, 800–1000°C, and 1000–2000°C. Within a temperature range of RT–130°C,

continuous lattice contraction of GO crystal occurs extensively owing to a mild vaporization of intercalated H_2O molecules. Within the range of 140–180°C, GO crystals are partially exfoliated because of the drastic vaporization of intercalated H_2O molecules. Within the 180–600°C temperature range, the interlayers for all GO and GP types are contracted with the removal of the main carboxyl groups. Within 600–800°C, a lattice relaxation of GP occurs owing to out-gassing generated from the residual carboxyl and partial hydroxyl groups, along with a broadening in FWHM. Within the 800–1000°C range, a large number of defects are generated owing to in-plane C=C cracking during the removal of the residual hydroxyl and partial epoxide groups. Within 1000–2000°C, a bottom-up layer stacking of GP as a crystal growth is observed with a decrease in the number of defects. The folding and unfolding processes of GO and GP are also observed at the boundaries of 140–600° and 800–1000°C, respectively. Furthermore, a partially reduced GO thin film can be applied as a catalytic thin film for a DSSC. These experimental results will be useful for the fundamental understanding of GO and GP, including the thickness control of GP and bottom-up layer stacking toward bulk graphite.

Appendix 1

XRD data for the GO/GP films and GO/GP powders

GO and GP thin films					GO and GP powders		
	Peak I		Peak II				
In situ measuring T(°C)	$^a d_{002}$ (Å)	^{b}FWHM (°)	$^c d_{002}$ (Å)	^{d}FWHM (°)	Annealing T(°C) (RT measuring)	$^e d_{002}$ (Å)	^{f}FWHM (°)
25	8.071	1.16			60	7.131	1.03
50	7.864	1.20			200	3.747	5.30
100	7.611	1.22			400	3.605	4.05
140	7.259	1.35	4.034	4.9	600	3.392	2.68
150	6.920	1.51	3.999	5.96	800	3.432	3.89
160	6.576	1.78	3.945	5.08	1000	3.498	4.60
170	6.053	2.32	3.903	5.16	1200	3.434	3.37
180	5.254	2.55	3.886	5.19	1400	3.427	1.65
190	4.990	1.93	3.829	5.17	1600	3.396	1.25
200	4.851	1.58	3.828	5.16	1800	3.393	1.10
250	4.553	1.49	3.791	5.05	2000	3.390	0.95
300	4.326	1.48	3.752	4.93			
400	4.029	1.41	3.666	4.62			
500	3.782	1.32	3.602	4.1			
600	3.593	1.2					
700	3.485	1.28					
800	3.433	1.55					
900	3.415	1.95					
1000	3.453	2.53					
25 after cooling	3.385	2.35					

error: $^a(\pm0.005)$, $^b(\pm0.2)$, $^c(\pm0.05)$, $^d(\pm0.3)$, $^e(\pm0.01)$, and $^f(\pm0.5)$.

5. Acknowledgements

6. References

Brodie, B. C. (1859). *Phil. Trans. R. Soc. A.* 149, 249–259.

Cullity, B. D. (1978). *Elements of X-ray diffraction*, 2nd Ed. Addison-Wesley.

Figueiredo, J. L.; Pereira, M. F. R.; Freitas, M. M. A. & Órfão, J. J. M. (1999). *Carbon* 37, 1379–1389.

Fujimoto, H. (2003). *Carbon* 41, 1585–1592.

Gao, W.; Alemany, L. B.; Ci, L. & Ajayan, P. M. (2009). Nature *Chemistry* 1, 403-408.

Geim, A. K. & Novoselov, K. S. (2007). *Nature Materials* 6, 183–191.

Giordano, F; Graziano, M. L. & Lesce, M. R. (1988). *J. Chem. Soc. Perkin Trans II* 5, 773–775.

Gosselin, P.; Bérard, A.; Mohrbach, H. & Ghosh, S. (2009). *Eur. Phys. J. C* 59, 883–889.

Graziano, G. (1998). *J. Chem. Soc. Faraday Trans* 94, 3345–3352.

Hirata, M.; Gotou, T.; Horiuchi, S.; Fujiwara, M. & Ohba, M. (2004). *Carbon* 42, 2929–2937.

Hummers, W. S. & Offerman, R. E. (1958). *J. Am. Chem. Soc.* 80, 1339–1339.

(a) Jeong, H. K.; Lee, Y. P.; Jin, M. H.; Kim, E. S.; Bae, J. J. & Lee, Y. H. (2009). *Chem. Phys. Lett.* 470, 255–258.

(b) Jeong, H. K.; Lee, Y. P.; Lahaye, R. J. W. E.; Park, M. H.; An, K. H.; Kim, I. J.; Yang, C. W.; Park, C. Y.; Ruoff, R. S. & Lee, Y. H. (2008). J Am Chem Soc 130, 1362–1366.

Ju, H. M.; Huh, S. H.; Choi, S. H. & Lee, H. L. (2010). *Mater. Lett.* 64, 357–360.

Kim, K. S.; Zhao, Y.; Jang, H.; Lee, S. Y.; Kim, J. M.; Kim, K. S.; Ahn, J.-H.; Kim, P.; Choi, J.-Y. & Hong, B. H. (2009). *Nature* 457, 706-710

Lee, C.; Wei X. D.; Kysar, J. W. & Hone, J. (2008). *Science* 321, 385–388.

Li, Z. Q.; Lu, C. J.; Xia, Z. P.; Zhou, Y. & Luo, Z. (2007). *Carbon* 45, 1686–1695.

Liu, Q.; Liu, Z.; Zhang, X.; Yang, L.; Zhang, N.; Pzn, G.; Yin, S.; Chen, Y. & Wei, J. (2009). *Adv. Funct. Mater.* 19, 894–904.

Lotya, M; Hernandez, Y.; King, P. J.; Smith, R. J.; Nicolosi, V.; Karlsson, L. S.; Blighe, F. M.; Zhiming Wang, S. D.; McGovern, I. T.; Duesberg, G. S. & Coleman, J. N. (2009). *J. Am. Chem. Soc.* 131, 3611–3620.

McAllister, M. J.; Li, J-L.; Adamson, D. H.; Schniepp, H. C.; Abdala, A. A.; Liu, J.; Herrera-Alonso, M.; Milius, D. L.; Car, R.; Prud'homme, R. K. & Aksay, I. A. (2007). *Chem. Mater.* 19, 4396–4404.

Mkhoyan, K. A.; Contryman, A. W.; Silcox, J.; Stewart, D. A.; Eda, G.; Mattevi, C.; Miller, S. & Chhowalla, M.(2009). *Nano Letters* 9, 1058–1063.

Obraztsov, A. N. (2009). *Nature Nanotechnology* 4, 212–213.

Stankovich, S.; Dikin, D. A.; Piner, R. D.; Kohlhaas, K. A.; Kleinhammes, A.; Jia, Y.; Wu, Y.; Nguyen, S. T. & Ruoff, R. S. (2007). *Carbon* 45, 1558–1565.

Stoller, M. D.; Park, S. J.; Zhu,Y.; An, J. H. & Ruoff, R. S. (2008). *Nano Lett.* 8, 3498–3502.

Titelman, G. I.; Gelman, V.; Bron, S.; Khalfin, R. L.; Cohen, Y. & Bianco-Peled ,H. (2005) *Carbon*, 43, 641–649.

Wang, X.; Zhi, L. & Mullen, K. (2008). *Nano Lett* 8, 323–327.
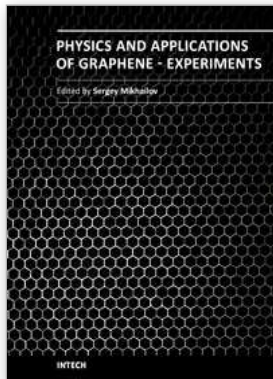
Physics and Applications of Graphene - Experiments

Edited by Dr. Sergey Mikhailov

The Stone Age, the Bronze Age, the Iron Age... Every global epoch in the history of the mankind is characterized by materials used in it. In 2004 a new era in material science was opened: the era of graphene or, more generally, of two-dimensional materials. Graphene is the strongest and the most stretchable known material, it has the record thermal conductivity and the very high mobility of charge carriers. It demonstrates many interesting fundamental physical effects and promises a lot of applications, among which are conductive ink, terahertz transistors, ultrafast photodetectors and bendable touch screens. In 2010 Andre Geim and Konstantin Novoselov were awarded the Nobel Prize in Physics "for groundbreaking experiments regarding the two-dimensional material graphene". The two volumes Physics and Applications of Graphene - Experiments and Physics and Applications of Graphene - Theory contain a collection of research articles reporting on different aspects of experimental and theoretical studies of this new material.

How to reference

In order to correctly reference this scholarly work, feel free to copy and paste the following:

Seung Hun Huh (2011). Thermal Reduction of Graphene Oxide, Physics and Applications of Graphene - Experiments, Dr. Sergey Mikhailov (Ed.), ISBN: 978-953-307-217-3, InTech, Available from: http://www.intechopen.com/books/physics-and-applications-of-graphene-experiments/thermal-reduction-of-graphene-oxide

INTECH
open science | open minds